A&A 670, A169 (2023)
https://doi.org/10.1051/0004-6361/202244456

Astronomy & Astrophysics

Imaging-spectroscopy of a band-split type II solar radio burst with the Murchison Widefield Array

Shilpi Bhunia[1,2], Eoin P. Carley[1], Divya Oberoi[3], and Peter T. Gallagher[1]

[1] Astronomy & Astrophysics Section, Dublin Institute for Advanced Studies, Dublin D02 XF86, Ireland
e-mail: bhunias@tcd.ie
[2] School of Physics, Trinity College Dublin, College Green, Dublin 2, Ireland
[3] National Centre for Radio Astrophysics, Tata Institute of Fundamental Research, Pune 411007, Maharashtra, India

Received 8 July 2022 / Accepted 25 November 2022

ABSTRACT

Type II solar radio bursts are caused by magnetohydrodynamic (MHD) shocks driven by solar eruptive events such as coronal mass ejections (CMEs). Often, both fundamental and harmonic bands of type II bursts are split into sub-bands, which are generally believed to be coming from upstream and downstream regions of the shock; however, this explanation remains unconfirmed. Here, we present combined results from imaging analyses of type II radio burst band splitting and other fine structures observed by the Murchison Widefield Array (MWA) and extreme ultraviolet observations from Solar Dynamics Observatory (SDO)/Atmospheric Imaging Assembly (AIA) on 28 September 2014. The MWA provides imaging-spectroscopy in the range 80−300 MHz with a time resolution of 0.5 s and frequency resolution of 40 kHz. Our analysis shows that the burst was caused by a piston-driven shock with a driver speed of $\sim$112 km s^{-1} and shock speed of $\sim$580 km s^{-1}. We provide rare evidence that band splitting is caused by emission from multiple parts of the shock (as opposed to the upstream–downstream hypothesis). We also examine the small-scale motion of type II fine structure radio sources in MWA images, and suggest that this motion may arise because of radio propagation effects from coronal turbulence, and is not due to the physical motion of the shock location. We present a novel technique that uses imaging spectroscopy to directly determine the effective length scale of turbulent density perturbations, which is found to be 1−2 Mm. The study of the systematic and small-scale motion of fine structures may therefore provide a measure of turbulence in different regions of the shock and corona.

Key words. techniques: imaging spectroscopy – Sun: activity – shock waves – turbulence

1. Introduction

Type II solar radio bursts are produced by magnetohydrodynamic (MHD) shocks driven by solar eruptive events such as coronal mass ejections (CMEs), flares, and jets (Nelson & Melrose 1985; Nindos et al. 2011; Gopalswamy et al. 2018; Zucca et al. 2018; Maguire et al. 2021; Jebaraj et al. 2021; Alissandrakis et al. 2021). The shock waves accelerate electrons, producing Langmuir waves and subsequently plasma emissions at the fundamental (f_p) and second harmonic ($2\,f_p$) of the plasma frequency, given by $f_p \approx 8980\sqrt{n_e}$, where n_e is electron number density (cm^{-3}). Often, the dynamic spectra of type II bursts exhibit various kinds of fine structure (FS). For example, the fundamental and harmonic bands of type II bursts drift to lower frequencies over time, and can sometimes split into sub-bands, known as 'band splitting'. Type IIs can exhibit FS on a variety of temporal and spectral scales, and altogether such structure can provide insight into shock kinematics, geometry, propagation, and turbulence in the solar atmosphere. Such properties are highly important for shock particle acceleration physics.

In a study based on 112 metric type II bursts, Vrsnak et al. (2001) reported that only 20% of type II bursts show the band-splitting phenomena. There is no information in the literature as to why such a small fraction of the type II bursts show such structure. Despite this small fraction, band splitting shows common features across different events. For example, the relative frequency split between the sub-bands $\triangle f/f$ is found to be within the range 0.1−0.5 and this value remains constant over the time duration of the event (Vrsnak et al. 2001).

It is still unclear what causes the band splitting of the type II bursts, but there are two widely accepted theories. The first popular mechanism was suggested by Smerd et al. (1974, 1975), whereby the high-frequency sub-band (HFS) and low frequency sub-band (LFS) of type II bursts are caused by coherent plasma emissions simultaneously coming from the downstream (behind) and upstream (ahead) regions of the black same shock front. This is commonly used to derive the shock compression ratio, Mach numbers (e.g. Vrsnak et al. 2001; Zucca et al. 2018; Maguire et al. 2020), and the coronal magnetic field strength (e.g. Kumari et al. 2017, 2019). There have been some imaging studies that have found evidence supporting this interpretation (e.g. Zimovets et al. 2012; Zucca et al. 2018; Chrysaphi et al. 2018). In these studies, band splitting was most often associated with a CME-driven shock, and the sub-band sources were closely spaced in imaging (Chrysaphi et al. 2018 reported the apparent spatial separation between two sub-band sources at 32 and 40 MHz for fundamental emission to be $\sim 0.2 \pm 0.05\,R_\odot$).

There have also been results that disfavour the upstream–downstream scenario. Du et al. (2014) found that the spectral features first appeared in the HFS seconds earlier than in the LFS, which according to the upstream–downstream scenario should have happened the other way around; that is, the spectral structures should first appear in LFS as the emission should first come from the low-density upstream (shock ahead) region. According to the review by Cairns (2011), in the downstream

region, the electron beam distributions are unstable to the production of enhanced Langmuir waves. Also, recent observations (Zucca et al. 2018; Magdalenić et al. 2020; Morosan et al. 2020; Kouloumvakos et al. 2021) of type II dynamic spectra show the burst having multiple sub-bands, which cannot be explained by the conventional upstream–downstream scenario. Therefore, an alternative mechanism can be used to explain the band-splitting phenomenon, where spatially separated parts of the shock front produce radio emissions at LFS and HFS (McLean 1967), although, as opposed to the upstream–downstream scenario, there is very little evidence supporting this theory (Zimovets & Sadykov 2015).

While type IIs band splitting is the most common fine structure, recent observations with modern instruments with excellent time, frequency, and angular resolution have revealed many different FSs in shock radio bursts (Magdalenić et al. 2020). These FSs are said to be a signature of the turbulence that shocks encounter while propagating through the inhomogeneous turbulent corona (Chen et al. 2018; Carley et al. 2021). The propagation effects modify the intrinsic properties (shape, size, positions, brightness temperature) of the observed radio source (Kontar et al. 2017, 2019; Sharma & Oberoi 2020; Zhang et al. 2021; Ryan et al. 2021; Murphy et al. 2021). There have been several studies (Fokker 1965; Steinberg et al. 1971; Riddle 1972; Zhang et al. 2021) modeling the extent of the scattering effects on the radio waves in the corona and some comparing the simulations with the observations of solar radio bursts (e.g. Kontar et al. 2019). There is currently ongoing debate over the length scales of turbulence that cause radio wave scattering. If the scattering happens where the spectrum is purely Kolmogorov-like, then the characteristic scale length of the density fluctuations is considered to be a combination of the inner and outer scale of the turbulence spectrum (Thejappa et al. 2007). Alternatively, it is also thought that the radio scattering happens near the inner scale. In the literature, there is no consensus on which length-scale to use (Bastian 1994), which is partly due to the lack of direct diagnostics of this effective length scale.

In this paper, we analyse a variety of fine-scale structures and fine-scale motions of type II radio bursts using the Murchison Widefield Array (MWA; Tingay et al. 2013). Firstly, we provide rare imaging of band splitting that does not agree with the upstream–downstream scenario, supporting the McLean (1967) model. Secondly, we developed a new technique that uses MWA imaging spectroscopy to examine fine-scale source motions of the type II burst and we show how we examined this in the context of coronal turbulence. Section 2 provides an observational overview of the type II burst and Sect. 3 describes the methods of the data analysis. The results and discussions are presented in Sects. 4 and 5, respectively, followed by conclusions in Sect. 6.

2. Observations

On 28 September 2014, a Geostationary Operational Environmental Satellite-15 (GOES-15)[1] M5.1 class solar flare started at 02:39:00 UT from the active region (AR) NOAA 12173 (Fig. 1a). This flare was also associated with a slow CME that was first seen by the Large Angle and Spectrometric Coronagraph C2 (LASCO; Brueckner et al. 1995) at 03:24:05 UT. According to the LASCO C2 CDAW[2] catalogue, the linear speed of the CME was 215 km s^{-1} on the plane-of-sky. This eruption event was observed in extreme ultraviolet (EUV) wavelengths by the Atmospheric Imaging Assembly (AIA; Lemen et al. 2012) on board the Solar Dynamics Observatory (SDO; Pesnell et al. 2012).

At 02:45 UT, the peak time of the X-ray flare, Learmonth Spectrograph[3] observed a type II burst, the radio signature of a shock during this eruptive event (Fig. 1b). The dynamic spectra show both the fundamental (f_p) and harmonic ($\sim 2\, f_p$) of the burst. Type II radio bursts often show band splitting (e.g. Vrsnak et al. 2001), where each of the fundamental and harmonic emissions are split into two sub-bands that show the same spectral drifts. We refer to these sub-bands as the HFS and LFS. Visually, it can be difficult to characterise the HFS and LFS in the type II harmonic band. To make the band splitting clearer, the Learmonth dynamic spectra were smoothed using a small kernel (2×2 pixels); see Fig. 1b. The fundamental band shows the clear band splitting where the HFS and LFS are indicated by F_U and F_L. We see the corresponding band splitting in the harmonic band, indicated by H_U and H_L. The drift rates computed for the two branches in the harmonic band are found to be very similar. The drift rates of the HFS and LFS are −0.160 and −0.158 MHz s^{-1}, respectively. We therefore conclude that the two observed sub-bands correspond to the band splitting often seen in type II radio bursts.

This type II burst was observed using the MWA, a low-frequency radio interferometer capable of providing a time and spectral resolution of 0.5 s and 40 kHz, respectively, across its 80−300 MHz observing band. The MWA observed the harmonic band of this radio burst in six different spectral pickets of 2.56 MHz bandwidth each. These observations spanned the frequency range 79.10−133.36 MHz with a spectral resolution of 40 kHz. These spectral bands of MWA observations are marked with black rectangular boxes on the Learmonth dynamic spectra in Fig. 1b.

3. Methods

High-fidelity solar radio images from the MWA data were obtained using the Automated Imaging Routine for Compact Arrays for the Radio Sun (AIRCARS; Mondal et al. 2019). AIRCARS is a self-calibration-based radio imaging pipeline optimised for spectroscopic snapshot imaging for centrally condensed arrays, such as the MWA. Its efficacy has been demonstrated in multiple recent works requiring high imaging quality and applications; for example, the first ever detection of m Solar Flux Unit (SFU)-level metrewave impulsive emissions from the quiet Sun (Mondal et al. 2020a), detection of spatially resolved gyrosynchrotron emission from CMEs (Mondal et al. 2020b), multiple investigations of quasi-periodic-pulsations in active solar radio emissions (Mohan et al. 2019a,b; Mohan 2021a,b; Mondal & Oberoi 2021), and development of precise absolute solar flux density calibration techniques (Kansabanik et al. 2022). Imaging and calibration was done using AIRCARS at a time resolution of 0.5 s and spectral resolution of 40 kHz for eight spectral channels in each of the six MWA spectral sub-bands. We applied independent gains obtained from self-calibration to each spectral channel.

Flux calibration was done using the fortuitous presence of Virgo-A in the very large field of view of the MWA. The flux density of Virgo-A at our frequencies of observation was obtained using a linear spectral fit to the data available from the

[1] https://space.oscar.wmo.int/satellites/view/goes_15
[2] https://cdaw.gsfc.nasa.gov/CME_list/nrl_mpg/2014_09/140928_c2.mpg
[3] Learmonth Observatory; https://www.sws.bom.gov.au/Solar/3/1

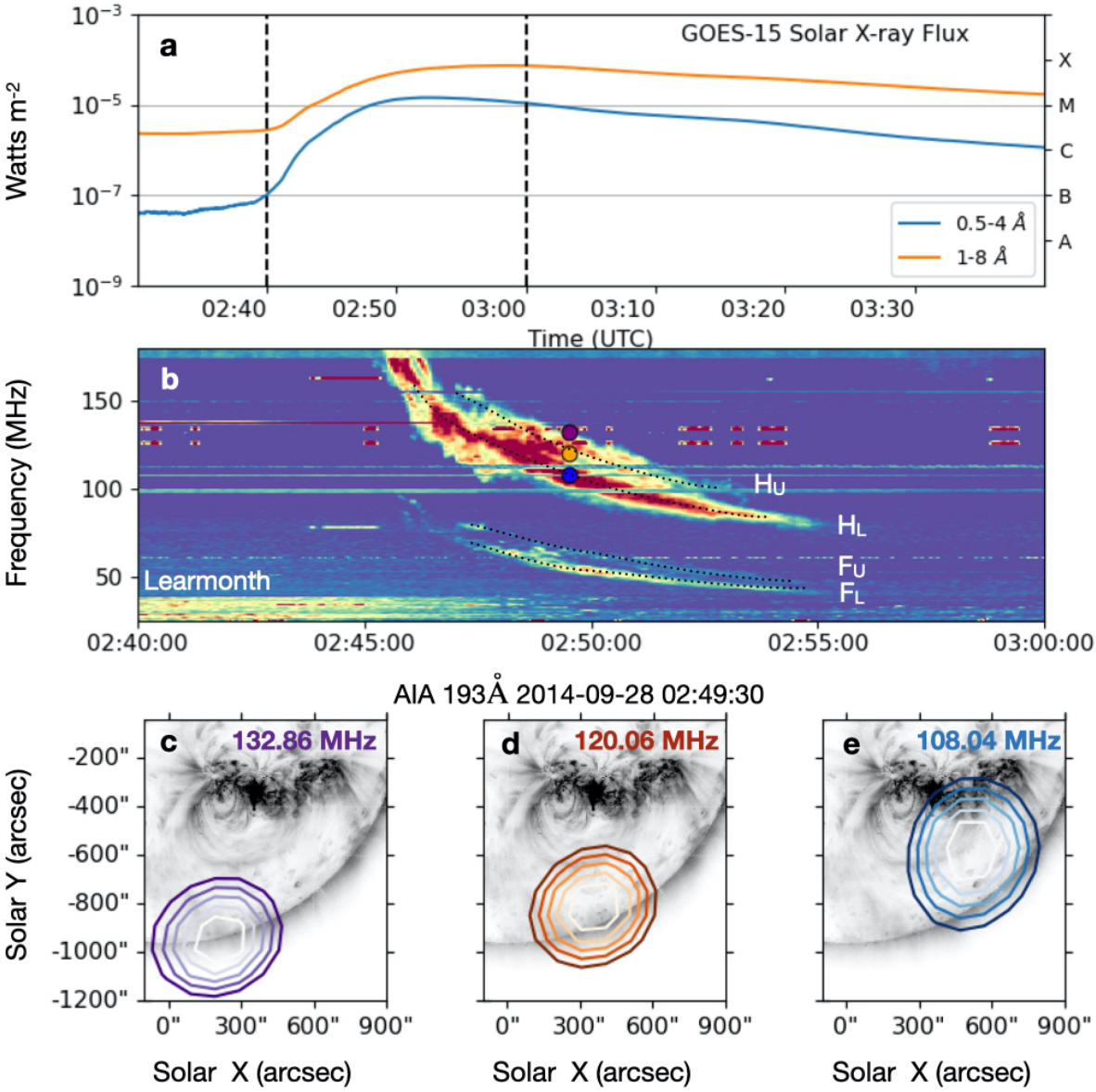

Fig. 1. Overview of the event observed by GOES-15, Learmonth, AIA and MWA. (a) GOES-15 light curves indicating a M5.1 class flare. The two vertical dashed lines show the time range of the Learmonth dynamic spectra. (b) Dynamic spectra of the type II radio burst observed by the Learmonth spectrograph. It is clear that the fundamental band shows band-spitting where the high- and low-frequency branches are indicated by F_U and F_L, respectively. The corresponding band splitting in the harmonic band is marked by H_U and H_L, respectively. (c)–(e) The three images show the position of MWA radio contours overlaid on the AIA 193 Å channel base image at 02:49:30 UT. The purple, orange, and blue contours are the MWA 132.86, 120.06, and 108.54 MHz contours (50%, 60%, 70%, 80%, and 90% of the peak intensity), respectively. These show the positions of the radio sources of different frequencies at the same time, indicated by purple, orange, and blue points on the Learmonth spectra.

NASA/IPAC Extragalatic Database[4] and a model for the MWA beam available from Sokolowski et al. (2017).

Figures 1c–e shows some example MWA radio images of the type II emission at 132.86 (purple), 120.06 (orange), and 108.54 (blue) MHz. The radio contours are overlaid on the AIA 193 Å base image of the eruption event at 02:49:30 UT. The frequencies and time of these radio sources are also marked on the Learmonth spectra as purple, orange, and blue circles, respectively. The radio contours show that the type II harmonic emissions have a single compact source that can be well described by a 2D elliptical Gaussian. A Gaussian model was therefore fitted to each of the AIRCARS images for all six spectral bands by doing chi-square minimisation using the Levenberg–Marquardt algorithm (Levenberg 1944; Marquardt 1963) and the parameters of the best-fit Gaussian models used to extract the information about the location, size, shape, and intensity of the burst emission. The fitting shows the emission source has a semi-major axis in the range 6′–10′ and a semi-minor axis within the range 5′–7′. The uncertainty in the position of the fit was calculated using CASA imfit software, which uses the standard method described in Condon (1997). According to this method, the uncertainty in position depends on the full width at half maximum (FWHM) of the major and minor axes, peak intensity, the rms noise, and the pixel width of the direction coordinate. The uncertainties in position are found to be very small, less than 1.2″, due to the high signal-to-noise ratio of the data. The

[4] NED; https://ned.ipac.caltech.edu

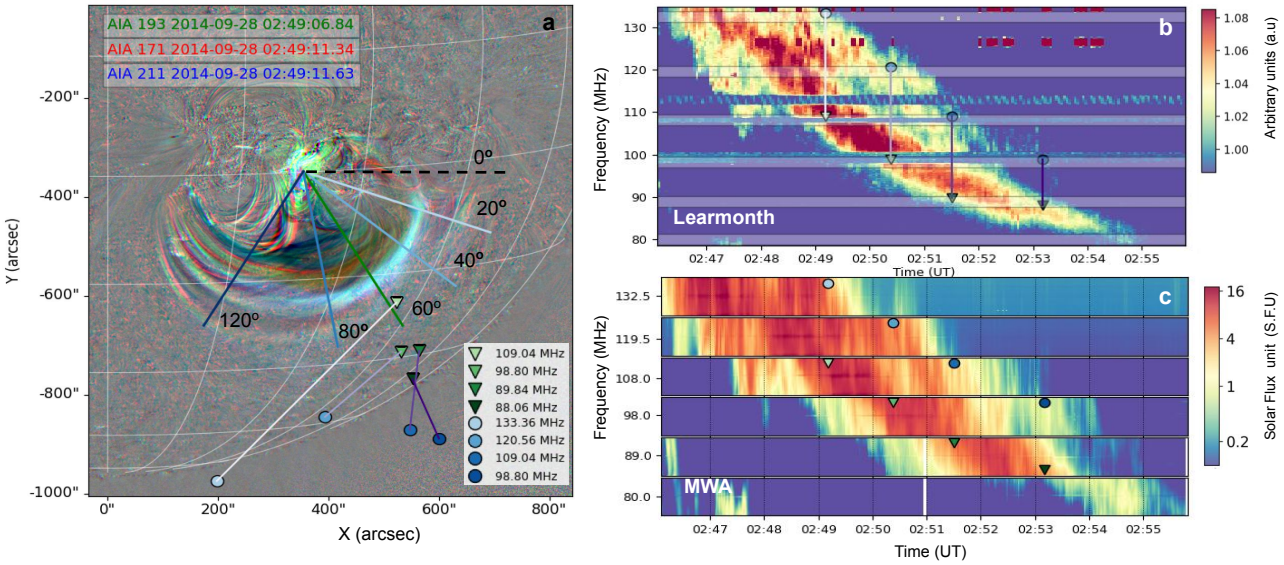

Fig. 2. Analysis of the band-split radio sources. (a) The ratio image of the eruptive event with SDO/AIA in 171, 193, 211 Å channels at 02:49:11 UT. The blue circle and green triangle points on the image are the position of radio sources of different frequencies at the same time from HFS and LFS, respectively (shown in panel b). The lines connect the HFS and LFS points at the same time. It is clear that both band sources are moving in different directions from each other and they are well separated in position. The top (b) and bottom (c) plots of the right panel show the Learmonth and MWA dynamic spectra of the type II harmonic band, respectively. The rectangular panels on the Learmonth spectra highlight the regions of the type II observed by MWA.

positional information from the Gaussian fits is used in the following sections to understand the kinematics of the split band sources and the fine-scale motion of type II bursts.

4. Results

4.1. Kinematics of the split-band radio sources

Figures 2b and c shows the harmonic band of the type II burst in the Learmonth and MWA spectra. Points of different frequencies at the same time have been chosen from the HFS (blue circles) and LFS (green triangle) of the harmonic band in the dynamic spectra. Figure 2a shows radio source positions (from the 2D Gaussian fits) of these frequencies and times overplotted on the AIA image, and a three-colour running ratio image of the eruption produced by AIA 171, 193, and 211 Å channels at 02:49:11 UT. Each AIA image was first normalised by its exposure time and the time difference in images for the ratio was ~3 min. The observations show that the LFS and HFS are spatially separated by up to around 485″ (~372 Mm), and get progressively closer at 157″ (~120 Mm) on the plane-of-sky (POS). The uncertainty in the position of the sources was considered to be the average position fluctuations of the radio sources, namely ~30″ (see Fig. 7). The separation of split-band sources occurring simultaneously is shown by the points connected by purple lines in Fig. 2a. The split-band sources also have noticeably different kinematics, with LFS (green triangles) propagating towards the southwest, which is the most prominent direction of the eruption, and HFS (blue circles) propagating in a lateral, east–west direction. Towards the end of the type II burst, the HFS is positioned at a greater radial distance (in the POS). The separation in space of the LFS and HFS by ~372 Mm is clearly indicative of the two radio sources being generated in different regions of the corona. This observation clearly contradicts the upstream–downstream scenario; for example, the HFS and LFS sources should be closely positioned in space and move in the same direction. In Sect. 5, we further discuss these source kinematics with regard to the various hypotheses for the band-splitting phenomena and explain that the source positions and separations that we observe do not support the upstream–downstream hypothesis for this event.

4.2. Large-scale kinematics of the shock

As part of the next step of our analysis, the speeds of the radio sources and the eruption event in EUV observations were calculated to understand the relationship between the eruptive active region and the type II burst (see Fig. 3). As the propagation of LFS sources was closely following the direction of the eruption event at around 60° (green line on the AIA ratio image in Fig. 2), these sources were chosen to calculate the speed of the radio sources.

The speed of the eruption in EUV was calculated in several directions indicated by lines in Fig. 2a at 20, 40, 60, 80, and 120° from the black dotted line (in the POS). The brightest point on the EUV front for these directions is chosen for each time using the point-and-click method. The distance of these points was calculated from the location of the active region origin and linear fits are performed over these distances using linear least-squares regression, as shown in Fig. 3. It was found that the speed of the EUV front is not the same in every direction and varies from 20 to 112 km s^{-1}. The uncertainty in the distance of these points is calculated from point-and-click uncertainty over several attempts. The eruption was most prominent towards 60°, where its speed was 112 ± 3 km s^{-1}.

The green triangles in Fig. 3 indicate the positions of the radio sources over time. For the position uncertainties for each radio source, the average fluctuation of the sources has been taken into account, which is ~0.5 arcmin or 23 Mm (Fig. 7). To determine the speed, the distance of the radio sources was calculated from the active region position and the linear regression was performed to get the speed of the radio sources and the error in the speed. The type II radio source speed (shock speed) is

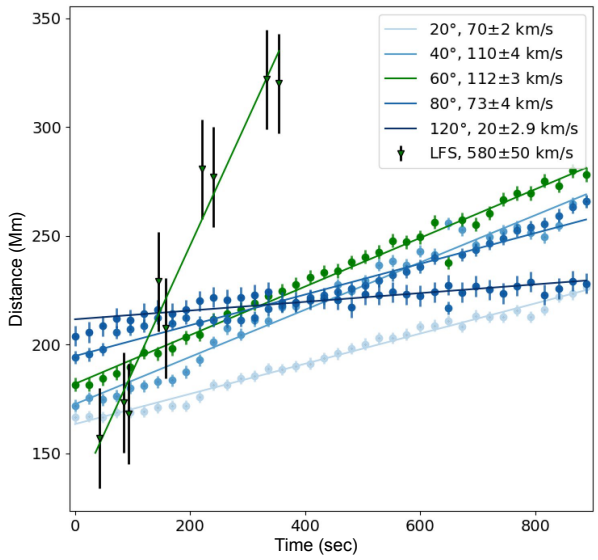

Fig. 3. Kinematics of the radio sources with respect to eruption. Given that the speed of the shock is much higher than the maximum speed of the eruption event, the shock originating this burst is expected to be a piston-driven shock, where the shock speed can exceed the driver speed.

found to be $580 \pm 50\,\mathrm{km\,s^{-1}}$, which is much faster than the maximum driver speed of $120\,\mathrm{km\,s^{-1}}$ observed in EUV[5].

Given the much larger shock speed compared to the driver speed, we expect that the shock causing this type II burst is the piston-driven mechanism (Vršnak & Cliver 2008; Nindos et al. 2011; Magdalenić et al. 2020). This is discussed further in Sect. 5.1.

4.3. Fine-scale motion of radio sources

Figure 4a shows the harmonic type II source motion at 133.22 (purple) and 133.36 (red) MHz with respect to the active region for the duration of the burst starting at 02:46:12 UT and ending at 02:49:50 UT. The background image is the three-colour ratio image of the eruption in AIA 193, 211, and 171 Å channels at 02:49:11 UT. Clearly, the fine-scale motion of the radio sources shows a complex chaotic behaviour. We describe this motion using the parameter $\Delta\theta$, the instantaneous change in source direction at time $t+1$ given by $\Delta\theta_{t+1} = \theta_{t+1} - \theta_t$. This direction change is expressed in radians and shown for each frequency channel (131.58, 131.74, 131.94, 132.08, 132.86, 133.02, 133.22, and 133.36 MHz) by the arrows on the dynamic spectra in Figs. 4b and c. The background dynamic spectra (grey scale) in both figures represent the peak amplitude of the Gaussian-fitted source at the corresponding frequency. Figure 4c shows a zoomed-in view of the region marked by the black rectangle in Fig. 4b. While the arrows indicate random instantaneous position changes at each time step, we observe that the position changes behave similarly for adjacent frequencies. This implies that the fine-scale motion is correlated across nearby frequencies. To investigate this systematic correlated behaviour, we produce a cross correlation of instantaneous direction and amplitude changes for sources in adjacent frequency channels. For example, $\boldsymbol{f}(t)$ represents the direction and magnitude of the instantaneous change in position over time for one frequency, while $\boldsymbol{g}(t)$ represents the same for another frequency. We use a dot-product correlation to look for correlated position changes (magnitude and direction) between nearby frequencies, given by

$$\boldsymbol{f} * \boldsymbol{g}(\tau) = \int \boldsymbol{f}(t) \cdot \boldsymbol{g}(t+\tau)\mathrm{d}t = \int f(t) g(t+\tau) \cos(\phi(t))\mathrm{d}t. \quad (1)$$

where $\phi(t)$ is the change of direction between $\boldsymbol{f}(t)$ and $\boldsymbol{g}(t)$. This equation shows a large response when the position shift direction and magnitude of the two time series for two different frequencies are the same. Figure 5 shows the dot-product correlation between 133.36 MHz and seven other frequencies (133.22, 133.02, 132.86, 132.08, 131.94, 131.74, and 131.58 MHz). The dashed line represents 3σ above the background noise for each of the correlation plot. We only consider there to be a significant correlation when the correlation peaks are above 3σ. We can see a significant correlation at zero time lag between 133.36 and 133.22 MHz. The correlation steadily drops with increasing frequency difference from 133.36 MHz and drops below significance beyond the nearest three frequencies.

In Fig. 6, we show the correlation strength as a function of frequency difference (Δf) for four coarse channels. The frequency difference (Δf) is the difference between the reference frequency (f_{ref}; chosen to be the highest frequency in the channel) and each frequency in the same channel used for the correlation. Each series of points (indicated by different colours) represents the correlation between f_{ref} and $f_{\mathrm{ref}} + \Delta f$ frequency for each different coarse channel. The colour scale of the circles for each coarse channel represents the Δf for eight frequencies in each channel. Clearly, the correlation strength decreases for larger Δf from f_{ref} for each coarse channel.

The phase calibration solutions are independent across frequency channels, and so we might naively assume the fine-scale motion among different frequency sources to be uncorrelated. However, a correlation is found to exist in fine-scale motion among nearby frequency channels and this correlation must have a physical cause in the corona. Section 5.2 discusses this physical cause and its potential relation to radio-source scattering in the corona due to turbulence.

Figure 7 shows histograms of the instantaneous position shift magnitude ($\Delta s_{t+1} = s_{t+1} - s_t$) of sources for a single frequency from all six coarse channels. The x-axis of all the plots is in log-space and a Gaussian has been fitted over the histogram for all channels to calculate the mean (black solid line) and standard deviation (black dotted line) of Δs. The distributions show a clear log-normal distribution in each coarse channel, and provide a clue to the potential physical cause of the stochastic motion observed in images, as discussed in Sect. 5.2.

5. Discussion

5.1. The mechanism responsible for band splitting in this type II event

In this work, we analyse a split-band metric type II burst that spatially and temporally relates to the eruption event on 28 September 2014, a M5.5 solar flare followed by a slow CME. The EUV observations of this event show the propagation of the expanding loops of the active region (Fig. 2, left panel). It is found that the disturbance caused by the expansion is not propagating uniformly in all directions and the maximum speed progressed towards the southwest at $\sim 112\,\mathrm{km\,s^{-1}}$. However, it should be noted that there is no direct evidence of the shock wave in the AIA observations. The direct evidence of this shock front, a split

[5] We note the POS CME linear speed was $215\,\mathrm{km\,s^{-1}}$ as reported by SOHO/LASCO CDAW catalogue. This speed deprojected by the active region angle from the sky plane is $\sim 430\,\mathrm{km\,s^{-1}}$.

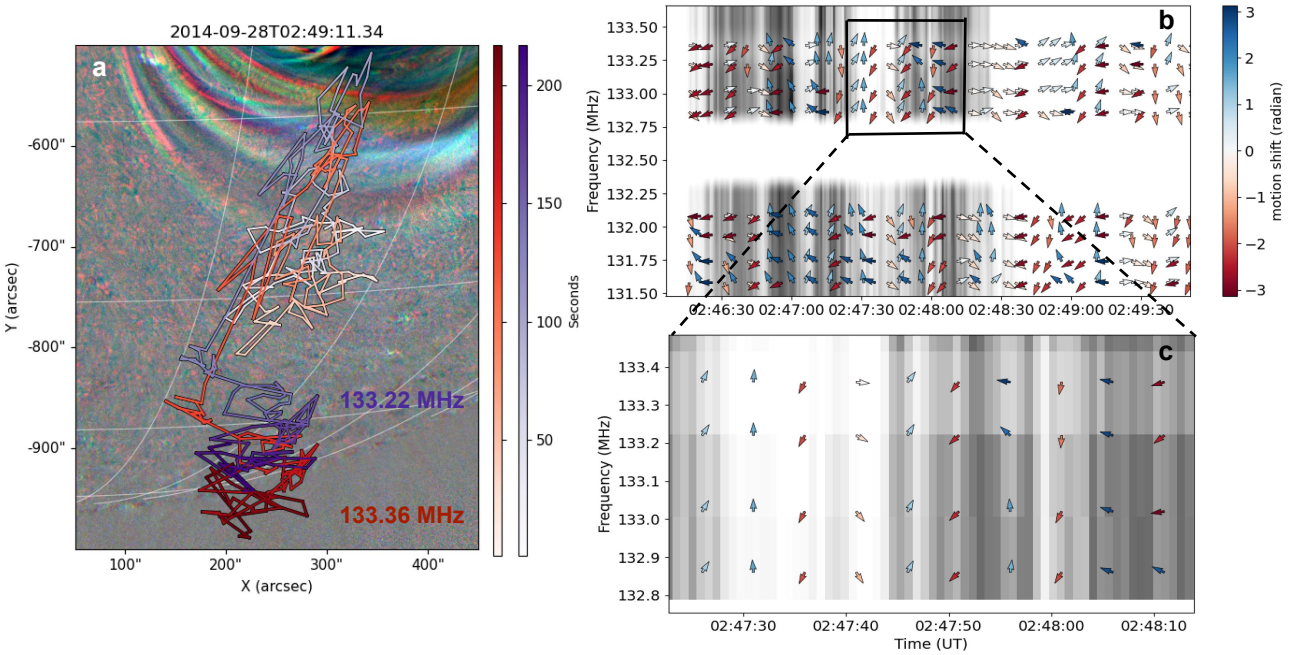

Fig. 4. Fine-scale motion of the radio sources. (a) The running ratio image of the eruption in AIA 193, 211, and 171 Å channels at 02:49:11 UT. The positions of the type II sources of 133.36 MHz (red) and 133.22 (purple) MHz are plotted over the image for a duration of 5 min, represented by red and purple bars, respectively. The dynamic spectra in panels b and c on the right show the peak amplitude of the Gaussian-fitted source. The arrows represent the instantaneous change in direction ($\theta_{i+1} - \theta_i$) of the source motion for different frequencies (131.58, 131.74, 131.94, 132.08, 132.86, 133.02, 133.22 and 133.36 MHz) in the channel. The blue arrows represent when the change in angle lies between 0 and π radians. Similarly, the red arrows represent when the change in direction lies between 0 and $-\pi$ radians. Panel c shows a zoomed-in view of the region marked in panel b. In panel c, one can see that, at each time point, the arrows point in almost the same direction across nearby frequency channels, exhibiting the correlated fine-scale motion.

band type II burst, was found in the dynamic spectra from the Learmonth observatory and the MWA.

The LFS sources are found to propagate in the same direction as the eruption and the speed of the radio sources is found to be around 580 km s^{-1}. This is considerably faster than the driver speed of ~112 km s^{-1} derived from the EUV observations. It is therefore likely that the shock associated with the eruption was a piston-driven shock (Vršnak & Cliver 2008). In such a scenario, a subsonic driver can cause a shock. The plasma is pushed outwards by a 3D piston impulsively, and the plasma ahead of the piston (expanding magnetic loops) cannot pass behind the driver. As a result, the shock 'races away' from the driver, and shock speed is greater than the driver speed. This is in contrast to the bow-shock scenario, in which plasma can pass behind the driver and the shock and driver speed are the same.

The high-fidelity interferometric imaging of MWA provides an important opportunity to image the source location of the split bands of type II bursts at the same time. There have only been a few studies that achieved this (Zimovets et al. 2012; Zucca et al. 2014; Zimovets & Sadykov 2015; Chrysaphi et al. 2018). This allows us to understand the cause of band splitting and also to compare the two widely accepted band-splitting theories. The most popular interpretation, based on the work of Smerd et al. (1974, 1975), is that the high- and low-frequency split bands are coming from downstream (behind) and upstream (ahead) regions of the shock front at the same time, respectively. The density compression across the shock leads to a separation of plasma frequency of upstream and downstream sources ($f_p \sim 8980\sqrt{n_e}$). Several evidence has been found in support of this interpretation (Chrysaphi et al. 2018; Zimovets et al. 2012; Zucca et al. 2014), but there have also been results that disfavour this upstream–downstream scenario. Du et al. (2014) found that the spectral features first appeared in the HFS seconds earlier than in the LFS, which, according to the upstream–downstream scenario, should happen the other way around. According to the upstream–downstream scenario, there should also be a strong correlation between the shock velocity and the frequency ratio between the sub-bands, but Du et al. (2015) show only a very weak or no correlation between these two parameters. Cairns (2011) also argues that in the downstream region, the absence of energetic electrons with respect to the ambient plasma does not lead to the growth of Langmuir waves in the region, which also disfavours the upstream–downstream scenario. An alternative mechanism was proposed by McLean (1967), whereby the band splitting originates because of multiple parts of the shock front encountering coronal environments of different physical properties, such as variations in electron density or magnetic field. There have been very few observational studies that support this view (Zimovets & Sadykov 2015).

In our analysis, it is observed that the apparent location of the split-band sources are initially rather far apart (~372 Mm in POS) and then become gradually closer with time (~120 Mm in POS). They also appear to move in different directions with time. For the reasons outlined below, the large observed spatial separation and their motion cannot be attributed to propagation effects alone. This emission is at the harmonic ($f = 2 f_p$), where the impact of the propagation effects is much less dramatic than at the fundamental. For instance, Zhang et al. (2021) show that, depending on the anisotropy and density fluctuations, a harmonic source at 35 MHz can suffer an absolute maximum position offset of ~0.1 $R_\odot$ (~69 Mm). The observed frequency range of the type II burst studied here is higher (79−134 MHz), implying that

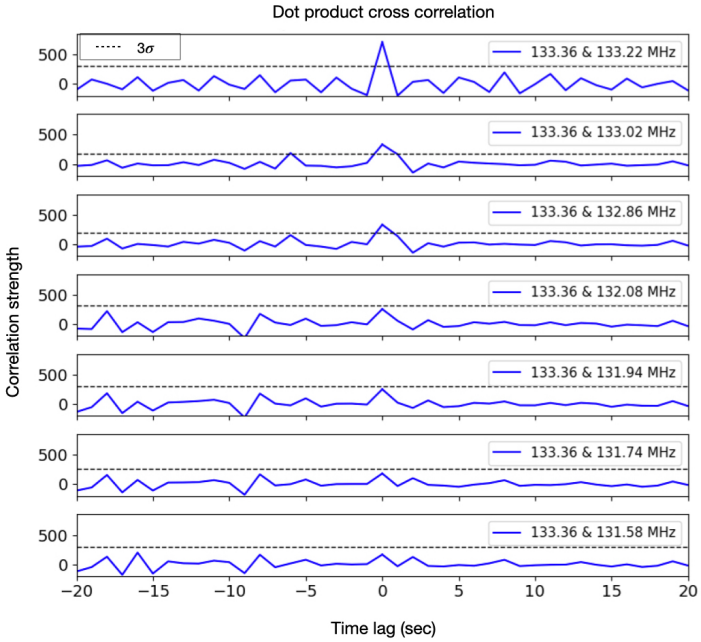

Fig. 5. Dot product correlation (blue) of the magnitude and $\Delta\theta$ between 133.36 MHz and seven other frequencies (133.22, 133.02, 132.86, 132.08, 131.94, 131.74, and 131.58 MHz). Dot product correlation represents a cross correlation of instantaneous direction and amplitude changes for sources in adjacent frequency channels. The dashed line represents the 3σ above the background noise for each of the correlation plots. We regard the correlation to be significant only if it exceeds 3σ. Clearly, there exists a significant correlation between the top three frequency pairs at zero time lag, which drops below 3σ level with increasing separation between frequencies.

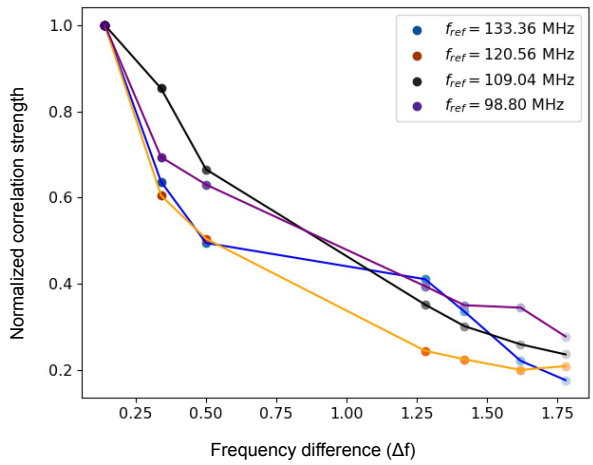

Fig. 6. Normalised correlation strength vs. frequency difference for all four coarse channels. Here the frequency difference (Δf) is the difference between the reference frequency ($f_{\rm ref}$) and each of the other frequencies for the dot-product cross correlation in MHz. For each channel, $f_{\rm ref}$ is chosen to be the highest frequency and each circle point represents the correlation strength between $f_{\rm ref}$ and each of the other frequencies in that channel. The correlation strength decreases with increasing Δf.

the propagation effects should be smaller still. Even when the propagation effects lead to large changes in the apparent locations and sizes of the observed sources (e.g. Sharma & Oberoi 2020), these changes are expected to be similar at nearby frequencies. The difference in observing frequencies for the HFS and LFS is not large; it lies in the range 10–20 MHz, leading to a $\Delta f/f \sim 15\%$. Despite their small spectral separation, the observed differences in locations and motions of the HFS and LFS sources are large. This implies that these differences cannot arise because of propagation effects alone and must come from these sources being intrinsically well separated.

To understand the differences in these regions in terms of the geometry of the magnetic field lines, the extrapolation of the field lines is done with the Potential Field Surface extrapolation (PFSS) model (Stansby 2019) using the Global Oscillation Network Group[6] (GONG) observations at 02:14 UT. The PFSS field lines are overlaid on the AIA image of the eruption event at 02:49:30 UT in the 193 Å channel in Fig. 8. Both sub-band sources of the type II burst are on different magnetic field loops, with the LFS closer to the active region core than the HFS. As discussed earlier, there can be a significant difference between the true and apparent positions of sources. However, it is clear from Fig. 8 that the separations are so large that these sources lie in different coronal environments.

This implies that the radio emissions must come from different parts of the shock-front, causing two sub-bands in the type II dynamic spectrum (Fig. 2b). The analysis by Zucca et al. (2018) and Kouloumvakos et al. (2021) also suggests a similar conclusion.

This is rare evidence against the upstream–downstream interpretation of split-band sources, which is commonly used to estimate the shock Mach number (Vrsnak et al. 2001) and the strength of the magnetic field (Kumari et al. 2017, 2019). Our work advocates against using such a diagnostic for split-band sources and reiterates the need for full imaging spectroscopy in interpreting type II fine structure.

5.2. The origins of the fine-scale motions

Figure 4 shows the complex motion of the type II sources over time. Our analysis shows that this motion, although disordered and random, exhibits a systematic correlation across nearby frequencies. Figure 5 shows that the source motion is well correlated across a bandwidth of 0.5 MHz for a specific spectral channel and this is true for all other channels. As discussed later in this section, the correlations in motion cannot arise because of calibration effects, as independent calibration solutions are applied to each frequency separately. This then poses the question of what causes disordered, instantaneous position shifts to be correlated across radio sources at nearby frequencies.

Recent studies show that low-frequency radio sources can appear to be displaced from their true location because of propagation effects arising from the density turbulence in the corona (e.g. Kontar et al. 2019; Zhang et al. 2021). Furthermore, previous studies showed that stochastic fluctuations in turbulent velocity fields can show a log-normal distribution (e.g. Arneodo et al. 1998; Mouri et al. 2009). For each frequency channel we observe here, the distribution of instantaneous magnitude changes in position (Δs_{t+1}) exhibits a log-normal distribution (Fig. 7). It is possible that the instantaneous and stochastic source displacements we observe here may arise from turbulent density fluctuations. For example, radiation at nearby frequencies launched from the same neighbourhood is expected to encounter approximately the same turbulent structures in the corona and consequently follow similar ray paths. We therefore interpret this observed correlation over small spectral spans as arising due to propagation effects like scattering and

[6] https://gong2.nso.edu/archive/patch.pl?menutype=s

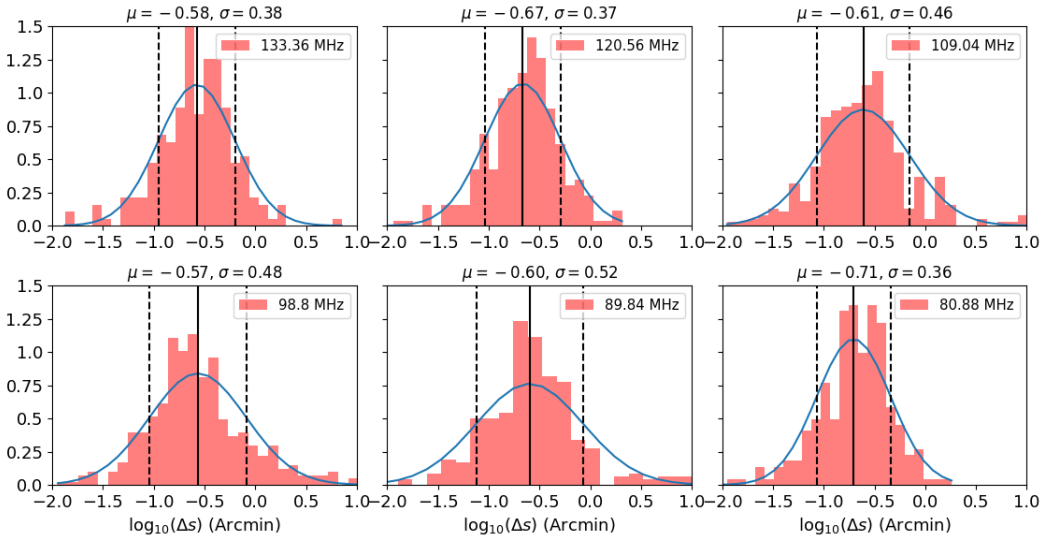

Fig. 7. Histogram showing the probability density of instantaneous magnitude changes in the position ($\Delta s_{t+1} = s_{t+1} - s_t$) of sources for a single frequency from all six channels. The blue curved line in each plot represents the Gaussian fitting done on the histogram. The mean and 1 sigma of the Gaussian are indicated as solid and dotted black lines, respectively.

refraction. An additional possibility is that these apparent motions are caused by small-scale local variations of the shock surface itself. Simulations show that a turbulent corona can cause a shock surface to become rippled and inhomogeneous, with shock properties such as shock strength and acceleration efficiency also being inhomogeneous (e.g. Andreopoulos et al. 2000; Zank et al. 2002; Lowe & Burgess 2003; Neugebauer & Giacalone 2005; Burgess 2006; Giacalone & Neugebauer 2008; Lu et al. 2009; Vandas & Karlický 2011; Guo & Giacalone 2010). If this is indeed the case, the root cause of the observed rapid and small-scale changes in the position of the emission is still the turbulence in the background corona. This implies that the observed spectral separation over which there is correlated motion carries information of the length scale of the coronal turbulence affecting the shock surface.

We relate the spectral separation of correlated fine channels to a spatial separation using a coronal electron density model, namely the Saito density model (Saito et al. 1970). A correlation among the fine channels separated by 0.5 MHz represents a correlation among radio sources separated in space by 1−2 Mm. We note that, although the absolute coronal heights might differ by larger amounts between different coronal electron density models, the differences between the coronal heights corresponding to two nearby frequencies are much smaller. For example, we followed the same procedure with the Newkirk density model (Newkirk 1961) and the resulting spatial separation is the same. Therefore, these numbers hold independent of the electron density model used. We interpret this as the correlation length scale of turbulence fluctuations. For example, there is a perturbation in the corona of 1−2 Mm, which causes an instantaneous position shift of radio sources with similar frequencies. If sources are separated by more than this length scale, the correlation disappears, as we show in Fig. 5.

There has been much debate in recent literature over the length scales of the coronal turbulence that causes radio wave scattering. For example, Bastian (1994) assume this scale length to be the inner-scale of coronal turbulence, on the order of 1−10 km in our case. However, Thejappa et al. (2007) theoretically determined this effective length scale to be $h = l_{\rm i}^{1/3} l_{\rm o}^{2/3}$, where $l_{\rm i}$ and $l_{\rm o}$ are the inner and outer scale, respectively. These

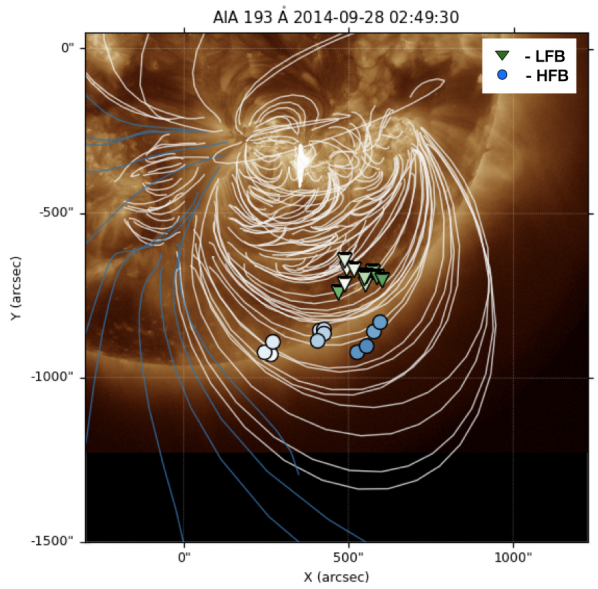

Fig. 8. Magnetic field lines extrapolated with the PFSS model overlaid on the region associated with the eruptive event on the AIA 193 Å image at 02:49:30 UT. In our region of interest, the field lines are mostly closed magnetic field loops (white). Clearly, LFS and HFS sources are associated with different loops.

latter authors use empirical expressions for these scales, with $l_{\rm i} = (r)^{\pm 0.1}$, where r is the heliocentric distance in units of solar radii and $l_{\rm o} = 8.82 \times 10^{-2} \left[\frac{R}{R_{\rm o}}\right]^{0.82}$ AU. Considering the heliocentric distance of the 133.36 MHz radio source to be 1.51 $R_\odot$ (according to a one-fold Saito density model), in our case these expressions lead to an effective scale length of $h \sim 0.7$ Mm, which is in the vicinity of our observationally determined scale length of 1−2 Mm. This provides evidence that the random fine-scale motion of radio sources in our observed type II radio burst is due to density turbulence, and that the scale length of Thejappa et al. (2007) applies in our case. Recent works (Chen et al. 2018; Carley et al. 2021) found the density turbulence spectrum to be

Kolmogorov like and Carley et al. (2021) found the spatial scales of the turbulence spectrum to range from 0.2 Mm to 62 Mm, placing our determined effective length scale in the inertial range of the turbulence.

5.2.1. Excluding other systematic effects for the fine-scale motion

While analysing the fine-scale motion of the type II sources, we have to be sure that these source motions are due to a coronal phenomenon (turbulence in our hypothesis) and not due to ionospheric effects or imaging analysis artifacts. Below we discuss the reasons why we can exclude these effects with confidence.

1. Ionospheric effects: While traversing the Earth's ionosphere, low-frequency radio sources can suffer apparent angular position offsets due to ionospheric propagation effects. It is conceivable that the observed correlated motion across nearby frequencies can arise from such effects. However, the timescale of the observed fluctuations, namely of about 1 s, is much faster than those associated with ionospheric variations (<50 s), (Jordan et al. 2017). Also, the position offsets due to ionospheric refraction are inversely proportional to f^2 (e.g. Loi et al. 2015), where f is the observing frequency. This implies that low-frequency radio waves will be affected more than high frequencies and also provides a quantitative scaling that should hold for ionospheric propagation effects. To check for this relationship, in Fig. 7 we show histograms of the instantaneous position shift magnitude ($\Delta s_{t+1} = s_{t+1} - s_t$) of sources for a single frequency from all six coarse channels. A Gaussian has been fitted to the histograms. The mean of the Gaussian model is shown by the black solid line and its σ is also shown. The $1/f^2$ trend expected due to ionospheric propagation is not seen in either of these quantities, implying that they are not likely to arise because of ionospheric propagation effects.
2. Imaging artifacts: During the process of imaging using self-calibration, it is possible for an arbitrary phase to be introduced that can then lead to position offsets in the image plane (Pearson & Readhead 1984). For the analysis presented here, the self-calibration for each of the different frequencies was done only for a single time slice and the solutions obtained were applied to the entire observing duration. In addition, self-calibration for each of the frequencies was done independently and the self-calibration-based position shifts were corrected by moving the centroid of the self-calibrated image to that of the image obtained prior to self-calibration. More importantly, a single arbitrary shift in the image plane due to self-calibration cannot give rise to the time varying shifts seen in these data in any case.
3. An independent check: Out of caution, we use the fortuitous presence of Virgo-A in the large MWA field of view to investigate the possibility of contamination from either or both of these effects. If the observed shifts correlated across nearby frequencies are a systematic effect arising from either the imaging process or ionospheric propagation, then a similar effect should also be seen for Virgo-A. An independent Gaussian model was fit to Virgo-A for each time and frequency slice. The location of the peak of the Gaussian model was subjected to analysis identical to that carried out for the location of the type II source. The position of Virgo-A was found to be very stable across time and frequency and no small-scale motions correlated across neighbouring frequencies could be found. This provides independent confirmation that the observed instantaneous position shifts in the type II emission are intrinsic and do not arise from any ionospheric propagation effects or imaging artifacts.

6. Conclusions

In the first part of this work, we investigate the mechanism by which shocks can cause split bands in the harmonic band of a particular type II event using imaging spectroscopy of MWA and EUV observations of AIA/SDO. Imaging the radio sources from these sub-bands reveals that the sources are separated in space by up to ~372 Mm in the plane of the sky. The radio emissions are likely generated in different coronal loops ahead of the shock front, generating plasma emission at different frequencies during the burst. This provides rare imaging evidence against the popular interpretation that the band splitting is caused by emission upstream and downstream of the shock front and calls into question the widespread use of this interpretation to calculate important properties such as the density jump across the shock, Mach number, and magnetic field. Our study demonstrates the importance of imaging for verifying which of these competing theories is behind the band splitting in type II solar bursts.

In the second part of the work, we used imaging spectroscopy to study the effect of small-scale perturbations to fine-scale motion of type II sources. At low radio frequencies, these perturbations are believed to arise due to coronal density inhomogeneities that the radiation encounters while propagating out through the corona. We observed that the fine-scale motion of the sources exhibited a systematic correlation across nearby frequencies. To investigate this, we developed a new technique of cross correlation of instantaneous changes in the direction and magnitude of the radio sources of nearby frequency channels (dot-product correlation). We interpret such correlations as arising because of small-scale density perturbations from coronal turbulence. These perturbations lead to similar displacement of sources at nearby frequencies spaced up to 0.5 MHz apart and corresponds to a spatial separation of ~1−2 Mm at coronal heights of interest. If this is interpreted as the effective length scale of turbulence, our observational work agrees with the theoretical findings of Thejappa et al. (2007).

Our work therefore provides a unique way to directly characterise the turbulence in different regions of shocks and the corona. One can also potentially obtain the intensity of these fine structures for a large range of frequencies and get the power density spectra, which can be used to gain insight into the spectral characteristics of coronal turbulence (Chen et al. 2018; Carley et al. 2021). Such studies can provide the range of length scales of the coronal density perturbations and provide an opportunity to check whether or not the determined length scale lies in the inertial range. This will be an interesting avenue to explore in future studies.

Acknowledgements. This scientific work makes use of the Murchison Radio-astronomy Observatory (MRO), operated by the Commonwealth Scientific and Industrial Research Organisation (CSIRO). We acknowledge the Wajarri Yamatji people as the traditional owners of the Observatory site. Support for the operation of the MWA is provided by the Australian Government's National Collaborative Research Infrastructure Strategy (NCRIS), under a contract to Curtin University administered by Astronomy Australia Limited. We acknowledge the Pawsey Supercomputing Centre, which is supported by the Western Australian and Australian Governments. S.B. is supported by the Hamilton PhD Scholarship at DIAS. E.P.C. is supported by the Schrödinger Fellowship at DIAS. D.O. acknowledges support of the Department of Atomic Energy, Government of India, under the project no. 12-R&D-TFR-5.02-0700. We would like to thank Dr. Peijin Zhang for his valuable discussions. This research has also made use

of NASA's Astrophysics Data System (ADS). This research has made use of the NASA/IPAC Extragalactic Database (NED), which is operated by the Jet Propulsion Laboratory, California Institute of Technology, under contract with the National Aeronautics and Space Administration. The authors would like to acknowledge AIA, GOES and Learmonth team for open access to their data. We thank the referee for the helpful comments to improve the paper.

References

Alissandrakis, C. E., Nindos, A., Patsourakos, S., & Hillaris, A. 2021, A&A, 654, A112
Andreopoulos, Y., Agui, J. H., & Briassulis, G. 2000, Annu. Rev. Fluid Mech., 32, 309
Arneodo, A., Manneville, S., & Muzy, J. 1998, Eur. Phys. J. B, 1, 129
Bastian, T. S. 1994, ApJ, 426, 774
Brueckner, G. E., Howard, R. A., Koomen, M. J., et al. 1995, Sol. Phys., 162, 357
Burgess, D. 2006, ApJ, 653, 316
Cairns, I. H. 2011, in The Sun, the Solar Wind, and the Heliosphere, eds. M. P. Miralles, & J. Sánchez Almeida, 4, 267
Carley, E. P., Cecconi, B., Reid, H. A., et al. 2021, ApJ, 921, 3
Chen, X., Kontar, E. P., Yu, S., et al. 2018, ApJ, 856, 73
Chrysaphi, N., Kontar, E. P., Holman, G. D., & Temmer, M. 2018, ApJ, 868, 79
Condon, J. J. 1997, PASP, 109, 166
Du, G., Chen, Y., Lv, M., et al. 2014, ApJ, 793, L39
Du, G., Kong, X., Chen, Y., et al. 2015, ApJ, 812, 52
Fokker, A. D. 1965, Bull. Astron. Inst. Neth., 18, 111
Giacalone, J., & Neugebauer, M. 2008, ApJ, 673, 629
Gopalswamy, N., Yashiro, S., Mäkelä, P., et al. 2018, ApJ, 863, L39
Guo, F., & Giacalone, J. 2010, ApJ, 715, 406
Jebaraj, I. C., Kouloumvakos, A., Magdalenic, J., et al. 2021, A&A, 654, A64
Jordan, C. H., Murray, S., Trott, C. M., et al. 2017, MNRAS, 471, 3974
Kansabanik, D., Mondal, S., Oberoi, D., Biswas, A., & Bhunia, S. 2022, ApJ, 927, 17
Kontar, E. P., Yu, S., Kuznetsov, A. A., et al. 2017, Nat. Commun., 8, 1515
Kontar, E. P., Chen, X., Chrysaphi, N., et al. 2019, ApJ, 884, 122
Kouloumvakos, A., Rouillard, A., Warmuth, A., et al. 2021, ApJ, 913, 99
Kumari, A., Ramesh, R., Kathiravan, C., & Wang, T. J. 2017, Sol. Phys., 292, 161
Kumari, A., Ramesh, R., Kathiravan, C., Wang, T. J., & Gopalswamy, N. 2019, ApJ, 881, 24
Lemen, J. R., Title, A. M., Akin, D. J., et al. 2012, Sol. Phys., 275, 17
Levenberg, K. 1944, Q. Appl. Math., 2, 164
Loi, S. T., Trott, C. M., Murphy, T., et al. 2015, Radio Sci., 50, 574
Lowe, R., & Burgess, D. 2003, Ann. Geophys., 21, 671
Lu, Q., Hu, Q., & Zank, G. P. 2009, ApJ, 706, 687
Magdalenić, J., Marqué, C., Fallows, R. A., et al. 2020, ApJ, 897, L15
Maguire, C. A., Carley, E. P., McCauley, J., & Gallagher, P. T. 2020, A&A, 633, A56
Maguire, C. A., Carley, E. P., Zucca, P., Vilmer, N., & Gallagher, P. T. 2021, ApJ, 909, 2
Marquardt, D. W. 1963, J. Soc. Ind. Appl. Math., 11, 431
McLean, D. J. 1967, PASA, 1, 47
Mohan, A. 2021a, ApJ, 909, L1
Mohan, A. 2021b, A&A, 655, A77
Mohan, A., McCauley, P. I., Oberoi, D., & Mastrano, A. 2019a, ApJ, 883, 45
Mohan, A., Mondal, S., Oberoi, D., & Lonsdale, C. J. 2019b, ApJ, 875, 98
Mondal, S., & Oberoi, D. 2021, ApJ, 920, 11
Mondal, S., Mohan, A., Oberoi, D., et al. 2019, ApJ, 875, 97
Mondal, S., Oberoi, D., & Mohan, A. 2020a, ApJ, 895, L39
Mondal, S., Oberoi, D., & Vourlidas, A. 2020b, ApJ, 893, 28
Morosan, D. E., Palmerio, E., Räsänen, J. E., et al. 2020, A&A, 642, A151
Mouri, H., Hori, A., & Takaoka, M. 2009, Phys. Fluids, 21, 065107
Murphy, P. C., Carley, E. P., Ryan, A. M., Zucca, P., & Gallagher, P. T. 2021, A&A, 645, A11
Nelson, G. J., & Melrose, D. B. 1985, in Type II Bursts, eds. D. J. McLean, & N. R. Labrum, 333
Neugebauer, M., & Giacalone, J. 2005, J. Geophys. Res. Space Phys., 110, A12
Newkirk, G., Jr. 1961, ApJ, 133, 983
Nindos, A., Alissandrakis, C. E., Hillaris, A., & Preka-Papadema, P. 2011, A&A, 531, A31
Pearson, T. J., & Readhead, A. C. S. 1984, ARA&A, 22, 97
Pesnell, W. D., Thompson, B. J., & Chamberlin, P. C. 2012, Sol. Phys., 275, 3
Riddle, A. C. 1972, PASA, 2, 98
Ryan, A. M., Gallagher, P. T., Carley, E. P., et al. 2021, A&A, 648, A43
Saito, K., Makita, M., Nishi, K., & Hata, S. 1970, Ann. Tokyo Astron. Obs., 12, 51
Sharma, R., & Oberoi, D. 2020, ApJ, 903, 126
Smerd, S. F., Sheridan, K. V., & Stewart, R. T. 1974, in Coronal Disturbances, ed. G. A. Newkirk, 57, 389
Smerd, S. F., Sheridan, K. V., & Stewart, R. T. 1975, Astrophys. Lett., 16, 23
Sokolowski, M., Colegate, T., Sutinjo, A. T., et al. 2017, PASA, 34, e062
Stansby, D. 2019, https://doi.org/10.5281/zenodo.2566462
Steinberg, J. L., Aubier-Giraud, M., Leblanc, Y., & Boischot, A. 1971, A&A, 10, 362
Thejappa, G., MacDowall, R. J., & Kaiser, M. L. 2007, ApJ, 671, 894
Tingay, S. J., Goeke, R., Bowman, J. D., et al. 2013, PASA, 30, e007
Vandas, M., & Karlický, M. 2011, A&A, 531, A55
Vršnak, B., & Cliver, E. W. 2008, Sol. Phys., 253, 215
Vrsnak, B., Aurass, H., Magdalenic, J., & Gopalswamy, N. 2001, A&A, 377, 321
Zank, G. P., Zhou, Y., Matthaeus, W. H., & Rice, W. K. M. 2002, Phys. Fluids, 14, 3766
Zhang, P., Wang, C., & Kontar, E. P. 2021, ApJ, 909, 195
Zimovets, I. V., & Sadykov, V. M. 2015, Adv. Space Res., 56, 2811
Zimovets, I. V., Vilmer, N., Chian, A. C. L., Sharykin, I., & Struminsky, A. 2012, A&A, 547, A6
Zucca, P., Pick, M., Démoulin, P., et al. 2014, ApJ, 795, 68
Zucca, P., Morosan, D. E., Rouillard, A. P., et al. 2018, A&A, 615, A89